The phonon dynamics of Sr_2RuO_4: microscopic calculation and comparison with that of La_2CuO_4

The phonon dynamics of Sr_2RuO_4: microscopic calculation and comparison with that of La_2CuO_4

Thomas Bauer and Claus Falter

Institut für Festkörpertheorie, Westfälische Wilhelms-Universität, Wilhelm-Klemm-Straße 10, 48149 Münster, Germany

E-mail: falter@uni-muenster.de

Abstract

The phonon dynamics of the low-temperature superconductor Sr_2RuO_4 is calculated quantitatively in linear response theory and compared with that of the structurally isomorphic high-temperature superconductor La_2CuO_4. Our calculation corrects for a typical deficiency of local density approximation-based calculations, which always predict too large an electronic k_z-dispersion insufficient for describing the c-axis response of real materials. With a more realistic computation of the electronic band structure, the frequency and wavevector dependent irreducible polarization part of the density response function is determined and used for adiabatic and nonadiabatic phonon calculations. Our analysis for Sr_2RuO_4 reveals important differences from the lattice dynamics of p- and n-doped cuprates. Consistently with experimental evidence from inelastic neutron scattering, the anomalous doping related softening of the strongly coupling high-frequency oxygen bond-stretching modes which is generic for the cuprate superconductors is largely suppressed or completely absent, respectively, depending on the actual value of the on-site Coulomb repulsion of the Ru 4d orbitals. Also the presence of a characteristic Λ_1 mode in La_2CuO_4 with a very steep dispersion coupled strongly to the electrons is not found for Sr_2RuO_4. Moreover, we evaluate the possibility of a phonon–plasmon scenario for Sr_2RuO_4, which has been shown recently to be realistic for La_2CuO_4. In contrast to the case for La_2CuO_4, in Sr_2RuO_4 the plasmons that are very low lying are overdamped along the c-axis.

1. Introduction

The discovery of superconductivity in Sr_2RuO_4 by Maeno *et al* [1] has attracted widespread attention partially because of the structural similarity with the cuprate-based high-temperature superconductors (HTSC's). While the mother compounds of the HTSC's are charge transfer insulators, and they usually need to be doped to become metallic and show superconductivity, in Sr_2RuO_4 low-temperature superconductivity at $T_c = 1.5$ K condenses from a metallic state that is a strongly two-dimensional Fermi liquid below about 20 K. The Fermi surface consists of three weakly corrugated cylindrical sheets α being hole-like and β and γ which are electron-like [2]. This is in contrast to La_2CuO_4 where only one Fermi sheet exists. The mechanism of conduction in Sr_2RuO_4 at higher temperatures is an interesting issue because the c-axis resistivity shows a broad maximum at around 130 K and for increasing temperatures the resistivity starts to decrease. In [3] such a metallic to nonmetallic crossover in the c-axis resistivity of a highly anisotropic metal like Sr_2RuO_4 with no corresponding feature in the ab-plane properties has been related to the strong coupling between the electrons and a bosonic mode propagating and polarized in c-direction, like the axial oxygen breathing mode O_z^Z, at the Z point of the Brillouin zone (BZ) to be discussed in section 3.

Superconductivity in Sr_2RuO_4 is thought to be of unconventional character and thus is intensively discussed in the literature. The current state of the experiments points to triplet superconductivity in Sr_2RuO_4 in contrast to the d-wave singlet pairing in the HTSC's. Most discussion of the superconducting mechanism for Sr_2RuO_4 is focused on magnetic fluctuations and Coulomb repulsion, for a

review see [4]. However, a contribution of electron–phonon interaction (EPI) to pairing may not be ruled out because the superconducting transition exhibits a clear isotope effect [5]. In case of the HTSC's there is increasing evidence that EPI is strong and phonons might play an important role for the electron dynamics, see [6, 7] and references therein.

Thus, a detailed theoretical study of phonon dynamics in Sr_2RuO_4 and a comparison with the situation in the HTSC's is desirable. The low-temperature superconductor Sr_2RuO_4 crystallizes in the K_2NiF_4 structure ($I4/mmm$) isostructural to the HTSC La_2CuO_4. An analysis and comparison of the lattice dynamics in both materials is the main intention of the present work. For this purpose we compute the phonon dynamics for Sr_2RuO_4 and oppose it with our earlier calculations for La_2CuO_4.

The most characteristic feature of phonon dynamics in the HTSC's is the strong softening upon doping of the high-frequency oxygen bond-stretching modes (OBSM) which seems to be generic for p- as well as n-doped cuprates, see [6–9]. The strong frequency renormalization and a related increase of the linewidths observed for these anomalous modes point to a strong coupling of the phonons to the charge dynamics. A discussion and theoretical investigations of these phonon anomalies are presented e.g. in [6–8, 10]. In agreement with inelastic neutron scattering [11] our calculations demonstrate that the typical OBSM phonon anomalies of the cuprates are not present in Sr_2RuO_4. Moreover the characteristic Λ_1 branch related to the strongly coupled O_z^Z mode in La_2CuO_4 is missing in Sr_2RuO_4.

In order to achieve reliable results for the Λ_1 phonon modes propagating and polarized along the c-axis a careful calculation of the proper polarization part of the density response function is crucial. This has already been shown for La_2CuO_4 in [12] where we have proven that the Λ_1 modes are highly sensitive with respect to the charge response perpendicular to the CuO plane. The large anisotropy of the electronic structure of the cuprates is as a rule considerably underestimated in DFT–LDA calculations and as a consequence the Λ_1 modes are not well described. So we have modified a LDA-based calculation for La_2CuO_4 to account for the much weaker k_z-dispersion of the electronic band structure in the real material.

We have optimized the interlayer coupling in such a way that the significant features of the sensitive Λ_1 phonons are well described. The same route is followed in the present work for Sr_2RuO_4 to get a realistic representation of the Λ_1 modes and in particular of O_z^Z which cannot be described in the ionic shell model taking additionally homogeneous electron gas screening into account [11].

Finally, we investigate the question if there is room for a phonon–plasmon scenario around the c-axis for Sr_2RuO_4 which has been shown to be a realistic option in La_2CuO_4 [12]. For a discussion of phonon–plasmon mixing in the cuprates in the context of many-body polaronic effects in the phonon spectrum we refer to [13]. Due to the much weaker electronic k_z-dispersion obtained in our computations as compared to La_2CuO_4, i.e. a much stronger anisotropy of Sr_2RuO_4, the calculated free-plasmon frequencies along the c-axis are about

a factor of eight smaller in the collisionless regime. Damping, generated by interactions between the electrons as well as interband transitions which are on a much lower energy scale as for La_2CuO_4 very likely leads to overdamping of the plasmons propagating strictly along the c-axis in Sr_2RuO_4. Thus, different from La_2CuO_4 coupled c-axis phonon–plasmon modes should not be well defined collective excitations at least strictly along the $\Lambda \sim (0, 0, 1)$ direction and accordingly do not enter the list of possible players for pairing in contrast to La_2CuO_4.

The paper is organized as follows. In section 2 the theory necessary to understand the calculated results is shortly reviewed. Section 3 presents the calculations. The modification of a LDA-based electronic band structure providing the basis of the single-particle content of the irreducible polarization part of the density response function is developed. Furthermore, the phonon dispersion is calculated in adiabatic approximation for Sr_2RuO_4 and a comparative discussion with the situation in La_2CuO_4 is given. Finally, in a nonadiabatic calculation the possibility of a phonon–plasmon scenario is examined. A summary of the paper is given in section 4 and the conclusions are drawn.

2. Theory and modelling

In the following a brief survey of the theory and modelling is presented. A detailed description can be found in [10] and in particular in [14] where the calculation of the coupling parameters of the theory is presented.

The local part of the electronic charge response and the EPI is approximated in the spirit of the quasi-ion approach [7, 15] by an *ab initio* rigid ion model (RIM) taking into account covalent ion softening in terms of (static) effective ionic charges calculated from a tight-binding analysis. The tight-binding analysis supplies these charges as extracted from the orbital occupation numbers Q_μ of the μ (tight-binding) orbital in question:

$$Q_\mu = \frac{2}{N} \sum_{n\mathbf{k}} |C_{\mu n}(\mathbf{k})|^2. \tag{1}$$

$C_{\mu n}(\mathbf{k})$ stands for the μ-component of the eigenvector of band n at the wavevector $\mathbf{k}$ in the first BZ; the summation in (1) runs over all occupied states and N gives the number of the elementary cells in the (periodic) crystal.

In addition, scaling of the short-ranged part of certain pair potentials between the ions is performed to simulate further covalence effects in the calculation in such a way that the energy-minimized structure is as close as possible to the experimental one [16]. Structure optimization and energy minimization is very important for a reliable calculation of the phonon dynamics through the dynamical matrix. Taking just the experimental structure data as is done in many cases in the literature may lead to uncontrolled errors in the phonon calculations.

The RIM with the corrections just mentioned then serves as an unbiased reference system for the description of the HTSC's and can be considered as a first approximation for

the insulating state of these compounds. Starting with such an unprejudiced rigid reference system nonrigid electronic polarization processes are introduced in form of more or less localized electronic charge fluctuations (CF's) at the outer shells of the ions. Especially in the metallic state of the HTSC's the latter dominate the *nonlocal* contribution of the electronic density response and the EPI and are particularly important in the CuO planes and the RuO plane. An essential nonlocal interaction of holes particularly with *c*-axis polarized optical phonons in the HTSCs has also been reported in [17, 18]. In addition, *anisotropic* dipole fluctuations (DF's) are admitted in our approach [14, 19], which prove to be specifically of interest for the ions in the ionic layers mediating the dielectric coupling and for the polar modes. Thus, the basic variable of our model is the ionic density which is given in the perturbed state by

$$\rho_\alpha(\mathbf{r}, Q_\lambda, \mathbf{p}_\alpha) = \rho_\alpha^0(r) + \sum_\lambda Q_\lambda \rho_\lambda^{\text{CF}}(r) + \mathbf{p}_\alpha \cdot \hat{\mathbf{r}} \rho_\alpha^{\text{D}}(r). \quad (2)$$

ρ_α^0 is the density of the unperturbed ion, as used in the RIM, localized at the sublattice α of the crystal and moving rigidly with the latter under displacement. The Q_λ and ρ_λ^{CF} describe the amplitudes and the form-factors of the CF's and the last term in equation (2) represents the dipolar deformation of an ion α with amplitude (dipole moment) $\mathbf{p}_\alpha$ and a radial density distribution ρ_α^{D}. $\hat{\mathbf{r}}$ denotes the unit vector in the direction of $\mathbf{r}$. The ρ_λ^{CF} are approximated by a spherical average of the orbital densities of the ionic shells calculated in LDA taking self-interaction effects (SIC) into account. The dipole density ρ_α^{D} is obtained from a modified Sternheimer method in the framework of LDA–SIC [14]. All SIC calculations are performed for the average spherical shell in the orbital averaged form according to Perdew and Zunger [20]. For the correlation part of the energy per electron the parametrization given in [20] has been used.

The total energy of the crystal is obtained by assuming that the density can be approximated by a superposition of overlapping densities ρ_α. The ρ_α^0 in equation (2) are also calculated within LDA–SIC taking environment effects, via a Watson sphere potential and the calculated static effective charges of the ions into account. The Watson sphere method is only used for the oxygen ions and the depth of the Watson sphere potential is set as the Madelung potential at the corresponding site. Such an approximation holds well in the HTSC's [16, 21]. Finally, applying the pair-potential approximation we get for the total energy:

$$E(R, \zeta) = \sum_{\mathbf{a}, \alpha} E_\alpha^{\mathbf{a}}(\zeta) + \frac{1}{2} \sum_{(\mathbf{a}, \alpha) \neq (\mathbf{b}, \beta)} \Phi_{\alpha\beta}(\mathbf{R}_\beta^{\mathbf{b}} - \mathbf{R}_\alpha^{\mathbf{a}}, \zeta). \quad (3)$$

The energy E depends on both the configuration of the ions $\{R\}$ and the electronic (charge) degrees of freedom (EDF) $\{\zeta\}$ of the charge density, i.e. $\{Q_\lambda\}$ and $\{\mathbf{p}_\alpha\}$ in equation (2). $E_\alpha^{\mathbf{a}}$ are the energies of the single ions. $\mathbf{a}$, $\mathbf{b}$ denote the elementary cells and α, β the corresponding sublattices. The second term in equation (3) is the interaction energy of the system, expressed in terms of *anisotropic* pair-interactions $\Phi_{\alpha\beta}$. Both $E_\alpha^{\mathbf{a}}$ and $\Phi_{\alpha\beta}$ in general depend upon ζ via ρ_α in equation (2).

The pair potentials in equation (3) can be separated into long-ranged Coulomb contributions and short-ranged terms, for details see e.g. [14].

From the adiabatic condition

$$\frac{\partial E(R, \zeta)}{\partial \zeta} = 0 \quad (4)$$

the electronic degrees of freedom ζ can be eliminated, an expression for the atomic force constants can be given and from this the dynamical matrix in harmonic approximation can be derived as

$$\begin{aligned} t_{ij}^{\alpha\beta}(\mathbf{q}) &= [t_{ij}^{\alpha\beta}(\mathbf{q})]_{\text{RIM}} \\ &\quad - \frac{1}{\sqrt{M_\alpha M_\beta}} \sum_{\kappa, \kappa'} [B_i^{\kappa\alpha}(\mathbf{q})]^* [C^{-1}(\mathbf{q})]_{\kappa\kappa'} B_j^{\kappa'\beta}(\mathbf{q}). \end{aligned} \quad (5)$$

The first term on the right-hand side denotes the contribution from the RIM. M_α, M_β are the masses of the ions and $\mathbf{q}$ is a wavevector from the first BZ.

The quantities $\mathbf{B}(\mathbf{q})$ and $C(\mathbf{q})$ in equation (5) represent the Fourier transforms of the electronic coupling coefficients and are calculated from the energy in equation (3), i.e.

$$\mathbf{B}_{\kappa\beta}^{\mathbf{ab}} = \frac{\partial^2 E(R, \zeta)}{\partial \zeta_\kappa^{\mathbf{a}} \partial R_\beta^{\mathbf{b}}}, \quad (6)$$

$$C_{\kappa\kappa'}^{\mathbf{ab}} = \frac{\partial^2 E(R, \zeta)}{\partial \zeta_\kappa^{\mathbf{a}} \partial \zeta_{\kappa'}^{\mathbf{b}}}. \quad (7)$$

κ denotes the EDF (CF and DF in the present model, see equation (2)) in an elementary cell. The $\mathbf{B}$ coefficients describe the coupling between the EDF and the displaced ions (bare electron–phonon coupling), and the coefficients C determine the interaction between the EDF. The phonon frequencies $\omega_\sigma(\mathbf{q})$ and the corresponding eigenvectors $\mathbf{e}^\alpha(\mathbf{q}\sigma)$ of the modes $(\mathbf{q}\sigma)$ are obtained from the secular equation for the dynamical matrix in equation (5), i.e.

$$\sum_{\beta, j} t_{ij}^{\alpha\beta}(\mathbf{q}) e_j^\beta(\mathbf{q}) = \omega^2(\mathbf{q}) e_i^\alpha(\mathbf{q}). \quad (8)$$

The equations (5)–(8) are generally valid and, in particular, are independent of the specific model for the decomposition of the perturbed density in equation (2) and the pair approximation in equation (3) for the energy. The lengthy details of the calculation of the coupling coefficients $\mathbf{B}$ and C cannot be reviewed in this paper. They are presented in [14]. In this context we remark that the coupling matrix $C_{\kappa\kappa'}(\mathbf{q})$ of the EDF–EDF interaction, whose inverse appears in equation (5) for the dynamical matrix, can be written in matrix notation as

$$C = \Pi^{-1} + \tilde{V}. \quad (9)$$

Π^{-1} is the inverse of the *proper polarization part* of the density response matrix and contains the kinetic part to the interaction C while $\tilde{V}$ embodies the Hartree and exchange–correlation contribution, because they are related to the second functional derivatives with respect to the density ρ of the kinetic energy and the exchange–correlation energy, respectively [10]. C^{-1} needed for the dynamical matrix and the EPI is closely related to the linear density response matrix and to the inverse dielectric matrix ε^{-1}, respectively.

Only very few attempts have been made to calculate the phonon dispersion and the EPI of the HTSC's using the linear

response method in form of density functional perturbation theory (DFPT) within LDA [22–25]. These calculations correspond to calculating Π and $\tilde{V}$ in DFT–LDA and for the *metallic* state only. On the other hand, in our microscopic modelling DFT–LDA–SIC calculations are performed for the various densities in equation (2) in order to obtain the coupling coefficients **B** and $\tilde{V}$. Including SIC is particularly important for localized orbitals like Cu 3d in the HTSC's. Our theoretical results for the phonon dispersion [6, 8, 19], which compare well with the experiments, demonstrate that the approximative calculation of the coupling coefficients in our approach is sufficient, even for the localized Cu 3d states. Written in matrix notation we get for the density response matrix the relation

$$C^{-1} = \Pi(1 + \tilde{V}\Pi)^{-1} \equiv \Pi\varepsilon^{-1}, \qquad \varepsilon = 1 + \tilde{V}\Pi. \quad (10)$$

The CF–CF submatrix of the matrix Π can approximatively be calculated for the metallic (but not for the undoped and underdoped) state of the HTSC's from a TBA of a single-particle electronic band structure. In this case the electronic polarizability Π in tight-binding representation reads:

$$\Pi_{\kappa\kappa'}(\mathbf{q}, \omega = 0) = -\frac{2}{N}\sum_{n,n',\mathbf{k}}\frac{f_{n'}(\mathbf{k}+\mathbf{q}) - f_n(\mathbf{k})}{E_{n'}(\mathbf{k}+\mathbf{q}) - E_n(\mathbf{k})}$$
$$\times [C_{\kappa n}^*(\mathbf{k})C_{\kappa n'}(\mathbf{k}+\mathbf{q})][C_{\kappa' n}^*(\mathbf{k})C_{\kappa' n'}(\mathbf{k}+\mathbf{q})]^*. \quad (11)$$

f, E and C in equation (11) are the occupation numbers, the single-particle energies and the expansion coefficients of the Bloch functions in terms of tight-binding functions.

The self-consistent change of an EDF at an ion induced by a phonon mode $(\mathbf{q}\sigma)$ with frequency $\omega_\sigma(\mathbf{q})$ and eigenvector $\mathbf{e}^\alpha(\mathbf{q}\sigma)$ can be derived in the form

$$\delta\zeta_\kappa^\mathbf{a}(\mathbf{q}\sigma) = \left[-\sum_\alpha \mathbf{X}^{\kappa\alpha}(\mathbf{q})\mathbf{u}_\alpha(\mathbf{q}\sigma)\right]e^{i\mathbf{q}\mathbf{R}_\kappa^\mathbf{a}} \equiv \delta\zeta_\kappa(\mathbf{q}\sigma)e^{i\mathbf{q}\mathbf{R}^\mathbf{a}}, \quad (12)$$

with the displacement of the ions

$$\mathbf{u}_\alpha^\mathbf{a}(\mathbf{q}\sigma) = \left(\frac{\hbar}{2M_\alpha\omega_\sigma(\mathbf{q})}\right)^{1/2}\mathbf{e}^\alpha(\mathbf{q}\sigma)e^{i\mathbf{q}\mathbf{R}^\mathbf{a}} \equiv \mathbf{u}_\alpha(\mathbf{q}\sigma)e^{i\mathbf{q}\mathbf{R}^\mathbf{a}}. \quad (13)$$

The self-consistent response per unit displacement of the EDF in equation (12) is calculated in linear response theory as:

$$\mathbf{X}(\mathbf{q}) = \Pi(\mathbf{q})\varepsilon^{-1}(\mathbf{q})\mathbf{B}(\mathbf{q}) = C^{-1}(\mathbf{q})\mathbf{B}(\mathbf{q}). \quad (14)$$

The generalization for the quantity Π in equations (9) and (10) needed for the kinetic part of the charge response in the nonadiabatic regime, where dynamical screening effects must be considered, can be achieved by adding $(\hbar\omega + i\eta)$ to the differences of the single-particle energies in the denominator of the expression for Π in equation (11). Other possible nonadiabatic contributions to C related to dynamical exchange–correlation effects and the phonons themselves are beyond the scope of the present approach. Using equations (10) for the dielectric matrix, ε, and the frequency dependent version of the irreducible polarization part, Π, according to equation (11), the free-plasmon dispersion is obtained from the condition,

$$\det[\varepsilon_{\kappa\kappa'}(\mathbf{q}, \omega)] = 0. \quad (15)$$
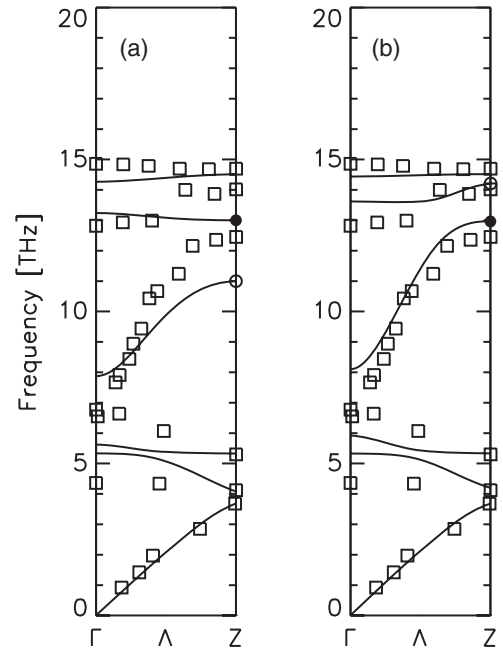

Figure 1. Calculated phonon dispersion for La$_2$CuO$_4$ of the *c*-axis polarized Λ_1 modes [12] based on the 31BM for the proper polarization part $\Pi_{\kappa\kappa'}$ (a) and the M31BM (b), respectively. The experimental data are represented as open squares ($\square$). The full dot ($\bullet$) denotes the O$_z^Z$ mode and the open circle ($\circ$) the A$_{2u}^Z$ (ferro) mode.

The coupled-mode frequencies of the phonons and the plasmons must be determined self-consistently from the secular equation (8) for the dynamical matrix which now contains the frequency ω implicitly via Π in the response function C^{-1}. Such a nonadiabatic approach is necessary for a description of the interlayer phonons and the charge response within a small region around the *c*-axis as performed in [6, 12] and in the present paper for Sr$_2$RuO$_4$.

3. Results and discussion

3.1. Modification of the LDA-based band structure for Sr$_2$RuO$_4$ and Λ_1 phonons

We shortly recall the construction of a modified LDA-based model for La$_2$CuO$_4$ which better describes the real anisotropy of the HTSC's that as a rule is not correctly represented in LDA being generally too isotropic. In our effort to obtain a reliable description of the Λ_1 phonons polarized and propagating along the *c*-axis of the cuprates [12] we have shown that these modes are highly sensitive with respect to details of the *c*-axis coupling and thus a very accurate representation of the electronic k_z-dispersion is needed. Typical LDA-based computations lead to an overestimation of the k_z-dispersion and give imprecise results for the Λ_1 modes.

In figure 1 we illustrate the degree of inaccuracy for the Λ_1 phonons, in La$_2$CuO$_4$ as obtained in [12]. Figure 1(a) shows the result of an LDA-based tight-binding representation of the electronic band structure (31 band model, 31BM) and figure 1(b) gives the outcome of a modified band structure
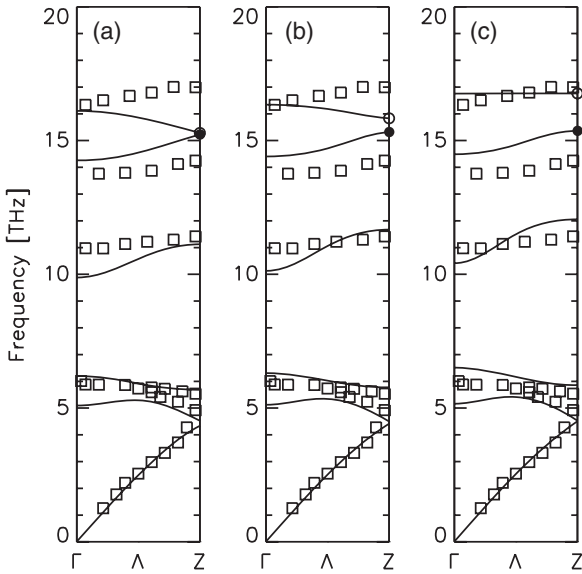
Figure 2. Calculated phonon dispersion for Sr_2RuO_4 of the Λ_1 modes based on different models for the electronic band structure as explained in the text. 27BM (a), M27BM1 (b) and M27BM2 (c). The experimental values from [11] are represented as open squares (□). The full dot (●) denotes the O_z^Z mode and the open circle (○) the A_{2u}^Z (ferro) mode.

(M31BM) with reduced first neighbour O_{xy}-La parameters of the 31BM by 1/6 and of the first neighbour La–La parameters by 1/3. As seen from figure 1 this leads to a much better result for the phonon modes. The characteristic experimental features of the dispersion i.e. the step-like structure of the second highest branch and most significant the third highest branch with the steep dispersion towards the Z point are not well reflected by the calculation with the 31BM as input for the proper polarization part in equation (11). Using, however, the M31BM the calculated phonon dispersion is in good agreement with the experiment as can be seen in figure 1(b). The characteristic features are now well described.

We also find as a consequence of the increased anisotropy in the M31BM a rearrangement of the three Z point modes with the highest energy. While in the 31BM the strongly coupling O_z^Z mode is the second highest mode and the A_{2u}^Z (ferro) mode the lowest one in the M31BM O_z^Z is the lowest and A_{2u} (ferro) the second highest of the three modes. Thus O_z^Z is the end point of the steep branch. During this mode rearrangement the

frequency of O_z^Z stays nearly constant while that of A_{2u}^Z (ferro) is strongly increased.

We have recalled these facts for La_2CuO_4 because for Sr_2RuO_4 a comparable high sensibility of the Λ_1 modes in dependence of the electronic k_z-dispersion occurs and an analogous mode behaviour for O_z^Z and A_{2u}^Z (ferro) results in response to a weaker k_z-dispersion. Likewise as in La_2CuO_4 this sensitivity of certain c-axis phonons is used to construct an accurate tight-binding description of the electronic band structure (BS) in Sr_2RuO_4.

As a first approximation for the BS we employ a tight-binding representation of the first principles linearized-augmented-plane-wave (LAPW) BS as obtained within the framework of DFT–LDA [26]. This analysis leads to a 27 band model (27BM) including Sr 4d, Ru 4d and O 2p states.

The associated calculated phonon dispersion for the Λ_1 modes of Sr_2RuO_4 along the $\Lambda \sim (0, 0, 1)$ direction is depicted in figure 2(a) and for the relevant Δ_1 and Δ_4 mode along the $\Delta \sim (1, 0, 0)$ direction in figure 3(a) together with the experimental data points [11]. Figures 2(b) and (c) and 3(b) and (c), respectively, display our results for two modified 27 band models (M27BM1 and M27BM2) with the tight-binding parameters important for c-axis is coupling (O_{xy}–O_z, Ru–Sr, O_{xy}–Sr, Ru–O_z) reduced by 1/2 and 1/5 with respect to the LDA-based 27BM. This leads as shown in figures 4(a)–(c) to a much stronger anisotropy as in the 27BM, i.e. to a strongly reduced k_z-dispersion which is also much weaker than in La_2CuO_4 [12].

In figure 4 the reduction of the electronic k_z-dispersion is shown along the cut of the Fermi surface (FS) highlighted in figure 5(a) when going from the 27BM to the most anisotropic M27BM2 via an intermediate c-axis coupling in M27BM1. The best result for the phonon modes in figures 2 and 3, which are less well described in the 27BM, are obtained for the highly anisotropic M27BM2, i.e. a nearly two-dimensional BS reflected by an even considerably weaker k_z-dispersion as in case of La_2CuO_4, see figure 6 and [12].

It is enlightening to point out that in context with the Δ_1 and Δ_4 branches in figure 3 an investigation of [11] exhibits that the dispersion cannot be described within a normal ionic shell model extended by homogeneous electron gas screening to simulate the metallic character of Sr_2RuO_4. Two specially adapted force constants between Ru–O_z and Ru–O_{xy} had to be introduced to mimic the observed dispersion. Of course these
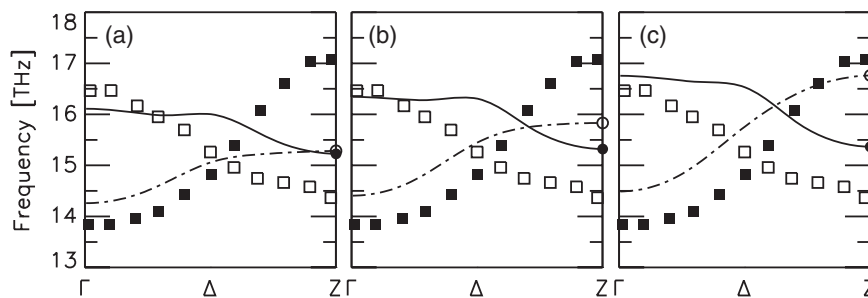

Figure 3. Calculated phonon dispersion for Sr_2RuO_4 of a Δ_1 mode (——) and a Δ_4 mode (— · —) based on the 27BM (a), the M27BM1 (b) and the M27BM2 (c). The experimental data points [11] are characterized by open squares (□) for Δ_1 and by full squares (■) for Δ_4. The full dot (●) and the open circle (○) at the Z point represent O_z^Z and A_{2u}^Z, respectively.
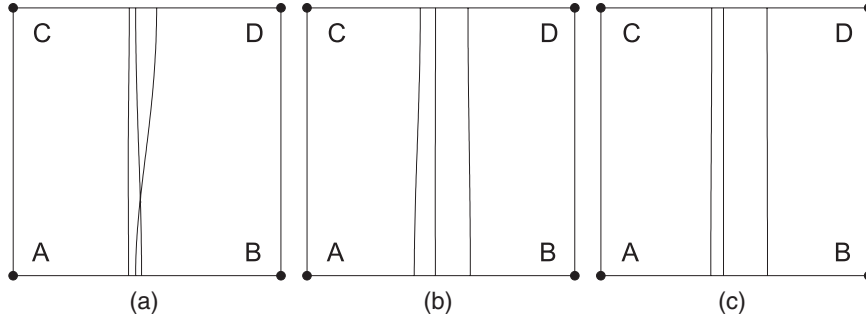
Figure 4. Electronic k_z-dispersion for Sr_2RuO_4 along the cut of the Fermi surface highlighted in figure 5(a) by the black bar. 27BM (a), M27BM1 (b) and M27BM2 (c). The corners of the surfaces are $A = (0.2, 0.2, 0)\frac{2\pi}{a}$, $B = (0.45, 0.45, 0)\frac{2\pi}{a}$, $C = (0.2\frac{2\pi}{a}, 0.2\frac{2\pi}{a}, \frac{2\pi}{c})$, $D = (0.45\frac{2\pi}{a}, 0.45\frac{2\pi}{a}, \frac{2\pi}{c})$.
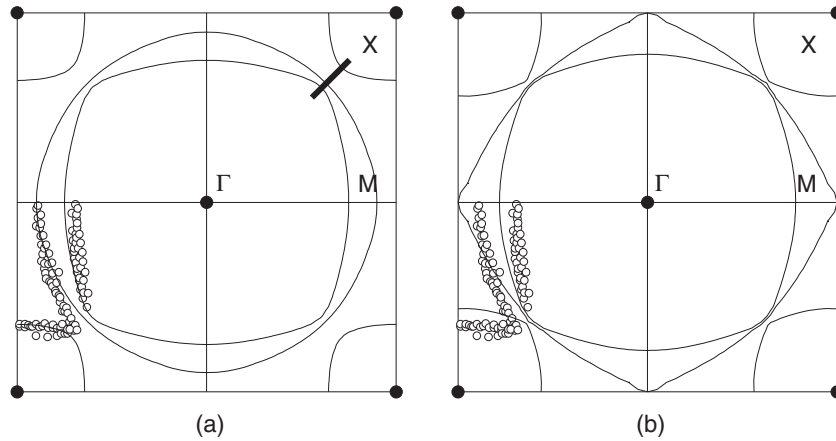

Figure 5. Comparison of the calculated multi-sheet Fermi surface of Sr_2RuO_4 in the $k_z = 0$ plane in model M27BM2 (a) and the 27BM (b) with the measured Fermi surface from [27]. The open dots (O) give the experimental results. For an explanation of the small black bar in (a) see figure 4.
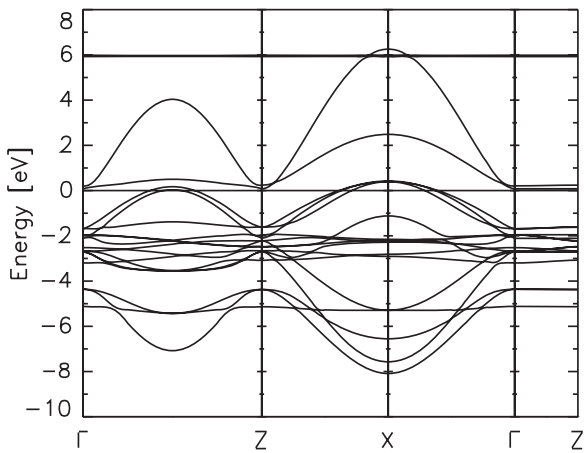

Figure 6. Electronic band structure $E_n(\mathbf{k})$ of Sr_2RuO_4 in the M27BM2 taking into account the strongly enhanced anisotropy of the real material as compared with the 27BM as a typical DFT–LDA-based model.

force constants do not have an intrinsic physical meaning. On the other hand, from our calculation we can conclude that on a microscopic level an accurate electronic dispersion along the c-axis is essential to understand the observed mode behaviour.

For a more detailed discussion of the rearrangement of the phonon modes in figures 2 and 3 as a result of a modification of the k_z-dispersion of the BS it is useful to display in figure 7 the displacement patterns of some phonon modes relevant for our studies.

In the 27BM the frequency of O_z^Z is nearly degenerate with A_{2u}^Z (ferro). We denote the latter mode as 'ferroelectric' because its displacement pattern looks similar to that of the ferro-like A_{2u}^Γ (ferro) mode at the Γ-point, see figure 7. Here the oxygen anions vibrate coherently against the cations in the lattice and as a consequence the electric dipole moments generated by the motion add constructively. With decreasing k_z-dispersion of the BS in M27BM1 and M27BM2 achieved by a reduction of the relevant tight-binding parameters mentioned above by 1/2 and 1/5, respectively, the frequency of A_{2u}^Z (ferro) increases by about 2 THz while O_z^Z remains virtually unchanged. This highly sensible behaviour with regard to c-axis coupling in Sr_2RuO_4 has also been demonstrated for La_2CuO_4 [12] where the frequency of A_{2u}^Z (ferro) increases by more than 3 THz as can bee read off from figure 1.

The physical origin for the sensitivity derives from the fact that for symmetry reasons in case of A_{2u}^Z (ferro) CF's can be excited in the screening process only at the ions in the ionic layers, i.e. O_z, La in La_2CuO_4 and O_z, Sr in Sr_2RuO_4.
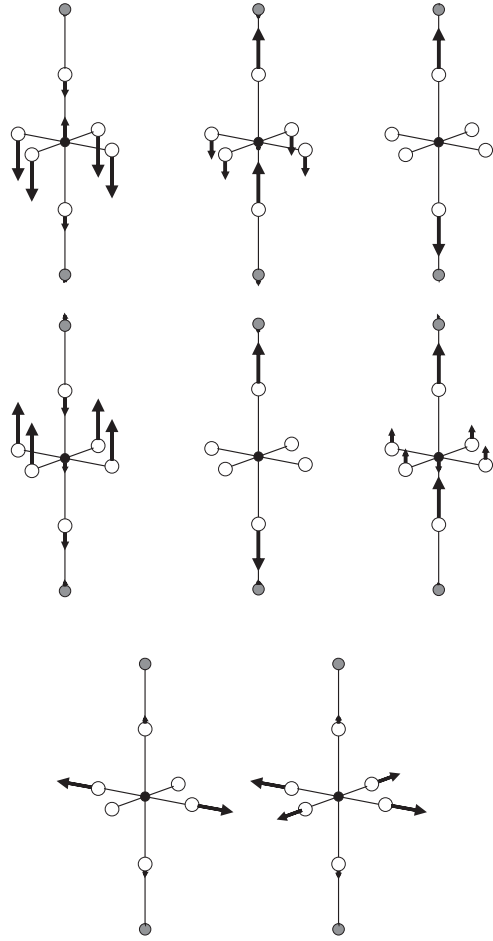
Figure 7. Displacement patterns of certain phonon modes relevant for the discussion of the phonon dynamics in Sr_2RuO_4. From left to right we display in the first row A_{2u}^Γ (ferro), $A_{2u}^\Gamma(\uparrow\downarrow)$, O_z^Γ; in the second row $A_{2u}^Z(\uparrow\downarrow)$, O_z^Z, A_{2u}^Z (ferro) and in the third row $\Delta_1/2$ and O_B^X.

Table 1. Magnitudes of the charge fluctuations $|\delta\zeta_\kappa|$ in units of 10^{-3} particles from equation (12) excited on the Ru 4d, O_{xy} 2p, O_z 2p and Sr 4d orbitals in the O_z^Z and A_{2u}^Z (ferro) mode. The results are given for comparison for the M27BM2 and the 27BM, respectively.

	O_z^Z				A_{2u}^Z (ferro)			
	Ru 4d	O_{xy} 2p	O_z 2p	Sr 4d	Ru 4d	O_{xy} 2p	O_z 2p	Sr 4d
M27BM	26.98	7.62	0.02	0.49	0	0	3.22	0.34
27BM	27.34	6.43	0.63	3.57	0	0	9.19	4.69

The strength of these CF's on the other hand is governed by the matrix elements of the proper polarization part $\Pi_{\kappa\kappa'}$ in equation (11) of the corresponding out-of-plane ions and, thus, depends critically on the coupling along the c-axis. Contrarily, the renormalization of O_z^Z is nearly exclusively given by the CF's on the Ru 4d and O_{xy} 2p orbitals in the plane. For quantitative results compare with the CF's listed in table 1. This explains the inertness of O_z^Z and the sensibility of A_{2u}^Z (ferro) with respect to the change of the electronic k_z-dispersion.

As a further example for the critical interrelation of c-axis phonon dynamics and electronic c-axis coupling we note that

the steep branch connecting A_{2u}^Γ (ferro) with O_z^Z in La_2CuO_4 is missing in Sr_2RuO_4. In the latter case due to mode rearrangement A_{2u}^Γ (ferro) as the lowest of the three highest modes at Γ is connected to $A_{2u}^Z(\uparrow\downarrow)$ that is the lowest of the three highest modes at Z and not to O_z^Z being the second highest mode.

The BS underlying the M27BM2 is illustrated in figure 6. As already mentioned the dispersion of the bands along the Λ (k_z) direction is extremely small, considerably smaller than for the 27BM and for the case of La_2CuO_4. Thus Sr_2RuO_4 is a nearly two-dimensional Fermi liquid. However, as our calculation in figures 2 and 3 have shown the remaining weak three-dimensionality is crucial to obtain a reliable description of certain c-axis phonons and the c-axis charge response in general.

Strong hybridization between Ru 4d and O_{xy} 2p states is evident from the BS in figure 6 because of the striking in-plane dispersion of the bands. Moreover, we find a similar shape of the partial density of states (PDOS) of the Ru 4d and the O_{xy} 2p orbitals around the Fermi energy ε_F. The states at ε_F are more strongly of Ru 4d type with some admixture of O_{xy} 2p. The contribution of O_z 2p and Sr 4d around ε_F is very small. In the M27BM2 we obtain for the PDOS at ε_F $Z_{Ru\ 4d}(\varepsilon_F) = 3.375$ eV^{-1}, $Z_{O_{xy}\ 2p}(\varepsilon_F) = 0.795$ eV^{-1}, $Z_{O_z\ 2p}(\varepsilon_F) = 0.002$ eV^{-1} and $Z_{Sr\ 4d}(\varepsilon_F) = 0.001$ eV^{-1}.

There are qualitative differences concerning the origin of hybridization comparing Sr_2RuO_4 with La_2CuO_4. Hybridization in Sr_2RuO_4 is strongly favoured because the radial extent of the 4d wavefunctions in Ru is much larger than for the 3d wavefunctions in Cu. Concurrently this leads to a weaker influence of electron correlation effects, e.g. a smaller on-site Coulomb repulsion U for Ru 4d compared to Cu 3d. In our calculations we find for U(Cu 3d) = 1.005 dRyd and for U(Ru 4d) = 0.619 dRyd. On the other hand, hybridization is promoted in La_2CuO_4 as compared to Sr_2RuO_4 because the energy levels of the copper and oxygen ions are close by in La_2CuO_4 but far off between ruthenium and oxygen in Sr_2RuO_4.

A further remarkable difference of the BS in Sr_2RuO_4 and La_2CuO_4 can be read off from figure 6 and the BS for La_2CuO_4 in [12]. In Sr_2RuO_4 up to three bands close to each other are crossing the Fermi level giving rise to a three-sheet FS while in La_2CuO_4 only one band is crossing and other bands are more far away. Thus we have a completely different situation as *interband transitions* are concerned which are on a much lower energy scale in Sr_2RuO_4 as in La_2CuO_4. So we find for $E_{n'}(\mathbf{k}+\mathbf{q}) - E_n(\mathbf{k})$ with $n' \neq n$ for $\mathbf{q}$ at the Z point in case of Sr_2RuO_4 a minimum of 20.67 meV in the M27BM2 around $\mathbf{k} = 0.68\frac{\pi}{a}(1,1,0)$, see also figure 6, while in La_2CuO_4 we obtain for the Z point at $\mathbf{k} = 0.42\frac{\pi}{a}(1,1,0)$ a minimum of 452.71 meV. This, of course, has important consequences for the contribution of the interband transitions to $\Pi_{\kappa\kappa'}$ in equation (11) concerning magnitude as well as energy scale.

For example the low energy scale of the interband transitions in Sr_2RuO_4 can generate damping of possible plasmons already at very low energy. Such a damping already present in the collisionless regime together with additional damping due to interactions between the electrons very likely

leads to overdamping of the very low lying plasmons in Sr_2RuO_4 along the c-axis. The energy of the latter in the collisionless regime is only 5–6 meV along the Λ direction as will be shown in section 3.3. Thus, the degree of the remaining weak three-dimensionality quantified by our computations is also very important for a possible existence of plasmons and coupled phonon–plasmon modes around the c-axis. Such modes have been predicted for La_2CuO_4 in our recent calculations [12] which, however, is not so anisotropic as Sr_2RuO_4 and the plasmons along the c-axis are at higher frequencies that overdamping can be avoided.

In figures 5(a) and (b), respectively, the calculated FS in the $k_z = 0$ plane is shown for the M27BM2 and the 27BM, together with the experimental data points [27]. The FS consists of the sheets α, β, γ. The α sheet is hole-like and β and γ are electron-like. The γ sheet is dominantly derived from the Ru $4d_{xy}$ orbitals, the α and β sheets are primarily related to the $4d_{xz}$ and $4d_{yz}$ orbitals of Ru which exhibit anticrossing behaviour along the zone diagonal. The large electron-like γ sheet passes right through the hybridization gap between the α and β sheets.

The experimental results are not well described by the 27BM in figure 5(b). In particular the crossing between the β and γ sheet in the 27BM which is typical for LDA calculations is experimentally not reproduced. This is really a crossing and not an anticrossing as for $k_z = 0$ the bands related to d_{xy} and d_{xz}/d_{yz} orbitals have different symmetry and no mixing is allowed. On the other hand, our modified BS model M27BM2 in figure 5(a) is in good agreement with the experimental FS.

In order to obtain also a more global impression of the magnitude of the enhanced anisotropy in the M27BM2 as compared to the 27BM we compare some FS parameters being important for transport like the Drude plasma energy tensor and the Fermi velocity tensor. The Drude tensor is defined as

$$\hbar\Omega_{\mathrm{p},ij} = \left(\frac{8\pi}{NV_z}\sum_{\mathbf{k}n}\delta(E_n(\mathbf{k})-E_\mathrm{F})v_{\mathbf{k}n,i}v_{\mathbf{k}n,j}\right)^{\frac{1}{2}} \quad (16)$$

and the Fermi velocity is given by

$$\langle v_{\mathrm{F},ij}^2\rangle^{1/2} = \left(\frac{2}{N}\sum_{\mathbf{k}n}\theta(E_\mathrm{F}-E_n(\mathbf{k}))v_{\mathbf{k}n,i}v_{\mathbf{k}n,j}\right)^{\frac{1}{2}}, \quad (17)$$

with

$$\mathbf{v}_{\mathbf{k}n} = \frac{1}{\hbar}\frac{\partial\,E_n(\mathbf{k})}{\partial\mathbf{k}}. \quad (18)$$

The output of our calculation for the 27BM and the M27BM2 is given in table 2. As can be seen we obtain a large enhancement of the anisotropy ratio for the plasma frequencies A_Ω and of the Fermi velocities A_{v_F} by about a factor 18 and 10, respectively, in the M27BM2 as compared to the LDA-based 27BM.

Additionally, we have included in table 2 the corresponding calculated data for La_2CuO_4 [12]. Again we recognize the by far larger anisotropy of Sr_2RuO_4 also in the transport properties. The values for $\Omega_{\mathrm{p},zz}$ and $\langle v_{\mathrm{F},zz}^2\rangle^{1/2}$ are significantly increased in La_2CuO_4.

Table 2. Calculated data for the Fermi surface parameters (Drude plasma energy tensor, Fermi velocity tensor) and the anisotropy ratio $A_\Omega = \Omega_{\mathrm{p},xx}/\Omega_{\mathrm{p},zz}$; $A_{v_\mathrm{F}} = \langle v_{\mathrm{F},xx}^2\rangle^{1/2}/\langle v_{\mathrm{F},zz}^2\rangle^{1/2}$ in the 27BM and M27BM2 for Sr_2RuO_4. For comparison the corresponding results are also given for La_2CuO_4 [12].

	$\hbar\Omega_{\mathrm{p},xx}$	$\hbar\Omega_{\mathrm{p},zz}$	$\langle v_{\mathrm{F},xx}^2\rangle^{1/2}$	$\langle v_{\mathrm{F},zz}^2\rangle^{1/2}$	A_Ω	A_{v_F}
27BM	1045.94	65.50	6.63	0.88	15.97	7.53
M27BM2	1017.40	3.57	6.03	0.08	284.99	75.38
M31BM	648.60	25.25	2.99	0.11	25.69	27.18

3.2. Phonon dynamics in Sr_2RuO_4—comparison with La_2CuO_4

In this section we investigate the phonon dynamics of Sr_2RuO_4 in the main symmetry directions $\Delta \sim (1, 0, 0)$, $\Sigma \sim (1, 1, 0)$ and $\Lambda \sim (0, 0, 1)$ and continue our discussion from section 3.1 of a comparison of important characteristics as found in our earlier calculations for La_2CuO_4.

For a definite investigation of the phonon renormalization induced by the *nonlocal* EPI effects of DF and CF type mediated by the second term in equation (5) a quantitative reference model for the calculation of the phonon dispersion not including the nonlocal screening effects but representing the important ionic component of binding in the material is needed. Such a model sketched in section 2 including approximately the *local* EPI effects is provided by the *ab initio* RIM extended via covalent ion softening and scaling of certain short-ranged pair potentials.

The result of the phonon dispersion along the main symmetry directions is shown for the RIM in figure 8 and compared with the experimental data from inelastic neutron scattering (INS) [11]. The static effective charges found for the model are $Ru^{2.7+}$, $O_{xy}^{-1.58}$, $O_z^{-1.67}$ and $Sr^{1.9+}$. In particular the charges of Ru and O_{xy} differ considerably from their nominal values Ru^{4+} and O^{2-}. This is due to the strong hybridization of the Ru 4d and O_{xy} 2p states that reduces the amplitude of the static effective charges in a mixed ionic–covalent compound like Sr_2RuO_4 because of the charge transfer (CT) from the cations to the anions is not complete as in the entirely ionic case. Consistent with the result of the effective ionic charges is an enhanced covalent character of the Ru–O_{xy} plane with a dominant covalent scaling of the Ru–O_{xy} potential and a more ionic character of the Sr–O_z layer with an ionic scaling of the Sr–O_z potential as found in the calculations.

Altogether the RIM with these modifications yields good structural data for the energy-minimized configuration. In detail we get for the planar lattice constant $a = 3.834$ Å, for the lattice constant along the c-axis $c = 12.625$ Å and for the internal position of the O_z and the Sr ion $z(O_z) = 0.163c$ and $z(Sr) = 0.142c$. The experimental values at 15 K are $a = 3.862$ Å, $c = 12.723$ Å, $z(O_z) = 0.162c$, $z(Sr) = 0.147c$ [28]. From these data we extract that the tetragonal distortion of the RuO_6 octahedra is significantly smaller than for the CuO_6 octahedra in La_2CuO_4. The ratio of the in-plane to out-of-plane distance of the oxygen is 0.9196 in Sr_2RuO_4 but 0.7706 in La_2CuO_4.

The phonon dispersion of the RIM is in reasonable agreement with the experiment as far as the branches with
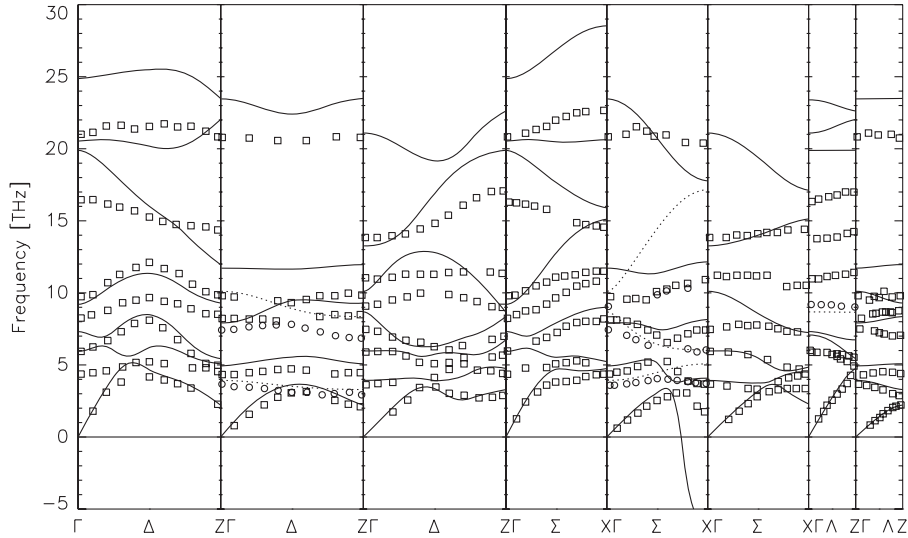
Figure 8. Calculated phonon dispersion of Sr_2RuO_4 for the RIM in the main symmetry directions $\Delta \sim (1, 0, 0)$, $\Sigma \sim (1, 1, 0)$ and $\Lambda \sim (0, 0, 1)$. The various symbols representing the experimental results are from [11] and indicate different irreducible representations. The arrangement of the panels from left to right according to the different irreducible representations is as follows: $|\Delta_1|\Delta_2(\cdots, \circ)$, $\Delta_4(\text{———}, \square)|\Delta_3|\Sigma_1|\Sigma_2(\cdots, \circ)$, $\Sigma_4(\text{———}, \square)|\Sigma_3|\Lambda_1(\text{———}, \square)$, $\Lambda_2(\cdots, \circ)|\Lambda_3|$. Imaginary frequencies are represented as negative numbers. The instability of the Σ_4-branch is discussed in the text.

lower frequencies are concerned. This points to the importance of the ionic component of binding in this material. Large deviations are observed for the modes with higher frequencies. In particular the high-frequency OBSM $\Delta_1/2$, O_B^X and O_z^Z, see figure 7, are not well described. The corresponding frequencies are overestimated as compared with the full calculation including DF's and CF's by about 5.8 THz, 7.4 THz and 6.7 THz, respectively. This can be attributed according to our approach to the missing screening of the Coulomb interaction by DF's and most importantly by CF's.

Noticeable is the soft Σ_4 mode at the X point and the very low frequency of the branch in the measurements (the notation for the irreducible representations characterizing the symmetry of the modes Σ_4 and Σ_3 is interchanged with the notation of [11]). This mode is associated with the rotation of RuO_6 octahedra around the c-axis. As indicated by our calculations the softness of the rotational mode can be considered as a precursor of a structural phase transition which in the meanwhile has been observed in the $Ca_{2-x}Sr_xRuO_4$ series [11]. From our calculation in the RIM this transition can be expected to be driven essentially by the strong component of the ionic forces in Sr_2RuO_4. Contrarily, Sr_2RuO_4 does not experience the tilt instability related to the Σ_3 branch at the X point found in our calculations for La_2CuO_4. This instability correctly indicates the experimentally observed structural phase transition from the high-temperature tetragonal (HTT) to the low-temperature orthorhombic (LTO) structure. Also this transition is mainly brought about by the long-ranged ionic forces.

Substituting the smaller isovalent Ca ions for the Sr ions induces a misfit between the Ca and Ru ions and generates a close connection between the rotation of the RuO_6 octahedra and the electronic and magnetic properties in the $Ca_{2-x}Sr_xRuO_4$ series [11]. Besides the softening of the

rotational mode in the range $0.5 \leqslant x \leqslant 1.5$ around $x \approx 0.5$ a similar structural transition occurs due to the softening of the RuO_6 tilt mode [29]. In this context it is interesting that at $x \approx 0.5$ in the paramagnetic phase of $Ca_{1.5}Sr_{0.5}RuO_4$ the γ Fermi sheet gains a remarkable k_z-dispersion and thus a more three-dimensional character than Sr_2RuO_4 [30]. This issue also emphasizes an interrelation between the electronic k_z-dispersion and the RuO_6 distortions.

In figure 9 we display the calculated results of the phonon dispersion admitting additionally to the RIM anisotropic DF's. This leads to a better agreement of the dispersion curves with the inelastic neutron results. Checking these calculations against the RIM the width of the spectrum is reduced towards the experiment. The frequencies of the transverse and longitudinal optical E_u modes polarized in the plane are decreased by the DF's and thereby the largest LO–TO splitting is reduced at the Γ-point from 8.8 THz in the RIM to 6.3 THz when dipolar polarization processes are included. At the same time the frequencies of the A_{2u} modes at Γ and Z are lowered considerably by the DF's in z-direction and the large splitting of the A_{2u}^Γ (ferro) mode of 10.13 THz in the RIM is reduced to 8.85 THz.

The high-frequency OBSM $\Delta_1/2$, O_B^X and O_z^Z are also decreased due to the screening by the DF's but are still overestimated by about 3.9, 5.1 and 4 THz as compared with the full calculation displayed in figure 10 including additionally CF's. Thus, the softening of these modes compared with the RIM is of the order 2–3 THz and the remaining effect of the renormalization can be assigned to the CF's on the Ru 4d and O_{xy} 2p orbitals.

The quantitative results for the CF's according to equation (12) are listed for the OBSM in table 3. The CF's for O_z^Γ are also given in the table which prove to be very different from those of O_z^Z despite the same local displacement pattern.
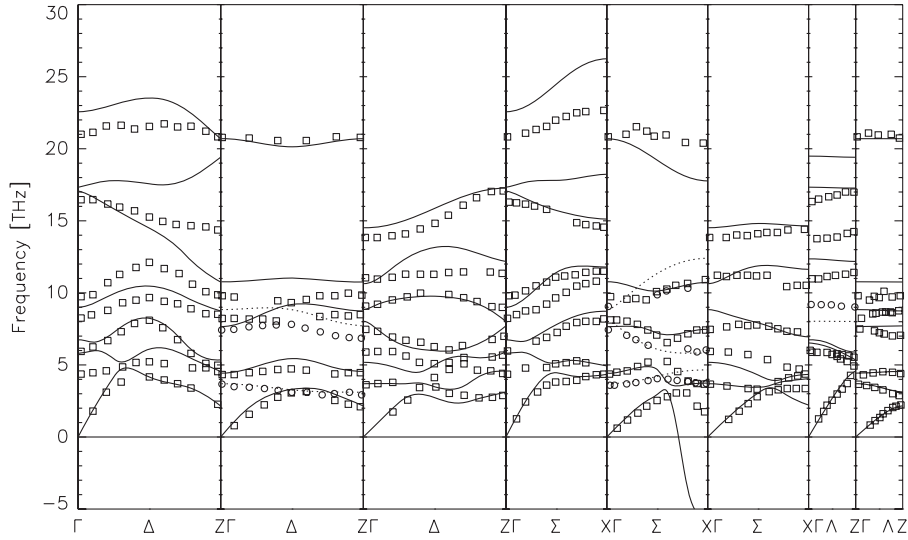
Figure 9. The same as in figure 8 but allowing additionally dipole fluctuations in Sr_2RuO_4. Imaginary frequencies are represented as negative numbers. The instability of the Σ_4-branch is discussed in the text.
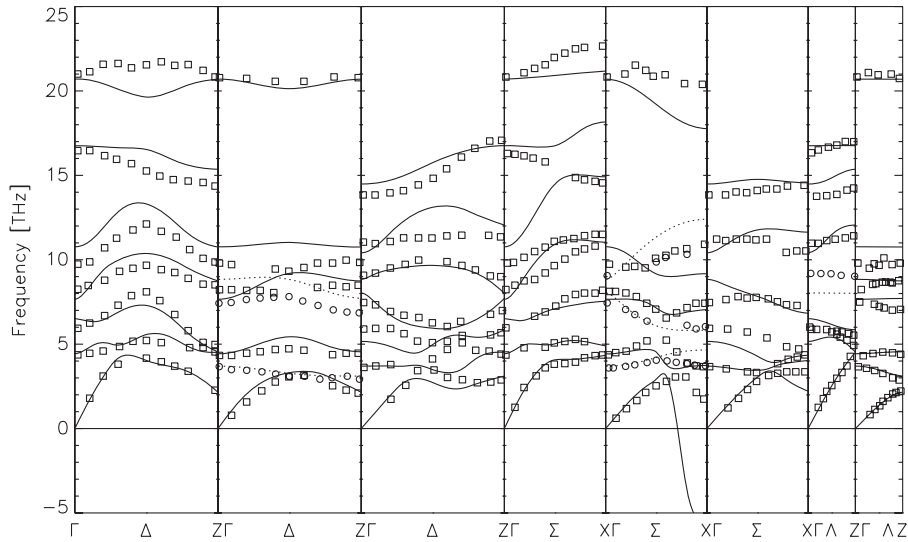

Figure 10. The same as in figure 8 but including additionally dipole fluctuations and charge fluctuations on the basis of the M27BM2 in adiabatic approximation. Imaginary frequencies are represented as negative numbers. The instability of the Σ_4-branch is discussed in the text.

As can be extracted from figure 7 for O_z^Γ and O_z^Z the apex oxygens O_z move locally in phase against or away from the RuO layers. Because of the weak screening along the c-axis and the corresponding large strength of the nonlocal EPI we can expect these vibrations to induce CF's in the RuO layers, see table 3 for the calculated results. However, the CF's differ qualitatively between O_z^Z and O_z^Γ, respectively, because for the Γ-point vibrations the following sum rule can be derived for the CF's $\delta\zeta_\kappa$ [10],

$$\sum_\kappa \delta\zeta_\kappa (\Gamma\sigma) = 0. \tag{19}$$

The sum over κ in equation (19) runs over the CF's in an elementary cell of the crystal and σ denotes the various eigenmodes at Γ. Physically equation (19) means that *local charge neutrality* of the elementary cell is maintained in

Table 3. Calculated charge fluctuations $\delta\zeta_\kappa$ in Sr_2RuO_4 in the M27BM2 excited on the Ru 4d, O_x 2p, O_y 2p, O_z 2p and Sr 4d orbitals and induced by the OBSM $\Delta_1/2$, O_B^X, O_z^Z and the O_z^Γ mode. For the displacement patterns compare with figure 7. Units are in 10^{-3} particles, a positive value means an accumulation of electrons.

	Ru 4d	O_x 2p	O_y 2p	O_z 2p	Sr 4d
$\Delta_1/2$	38.252	0	4.472	−0.002	0
O_B^X	50.875	0	0	0.119	0.081
O_z^Z	26.984	7.621	7.621	0.022	0.486
O_z^Γ	12.521	−3.714	−3.714	−2.224	−0.319

the long-wavelength limit ($\mathbf{q} \rightarrow \mathbf{0}$), i.e. the mode-induced CT is organized within the cell such that from the outside the cell looks electrically neutral. Equation (19) puts a
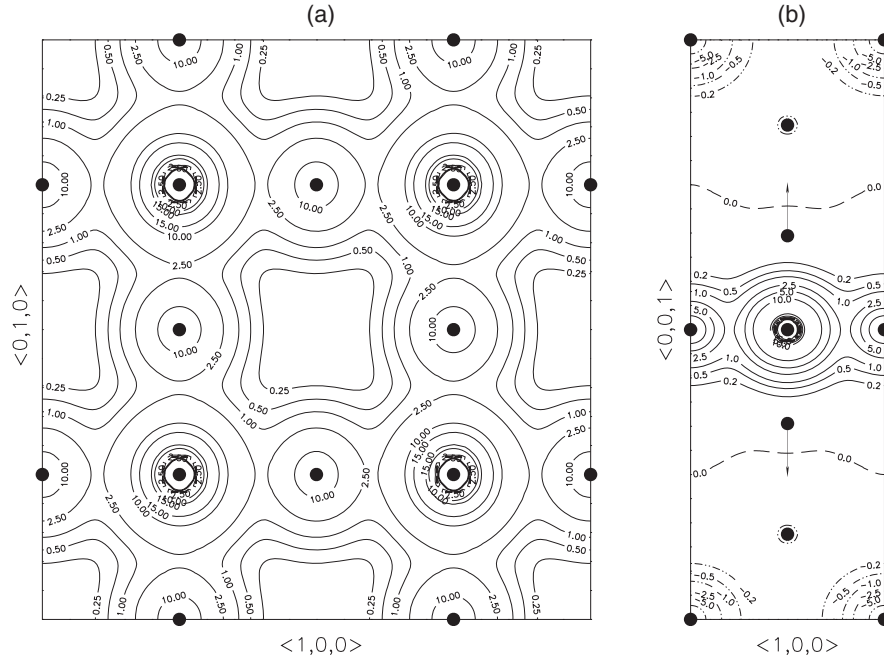
Figure 11. Contour plot in the RuO plane (a) and perpendicular to the RuO plane (b) of the nonlocal part of the displacement-induced charge density redistribution for the O_z^Z mode calculated according to equation (20) for the M27BM2. The units are in $10^{-4} e^2/a_B^3$. The phase of O_z^Z is as in figure 7. Full lines (——) indicate accumulation of electrons in the corresponding region of space and broken lines ($-\cdots-$) indicate regions of repulsion for the electrons.

strong constraint on the possible CT in the cell and thus on the screening by CF's. This restriction explains the small renormalization of the frequency of only 0.581 THz of O_z^Γ in relation to O_z^Z where the renormalization due to CF's is 4.046 THz. In [11] the pronounced softening and the broadening of O_z^Z is attributed to a strong coupling between this phonon and an interlayer charge transport. Such an interpretation is supported by our calculations for O_z^Z where the CF's can be read off from table 3 and the CT is illustrated in figure 11 in terms of the nonlocal part of the displacement-induced rearrangement of the charge density according to

$$\delta\rho_n(\mathbf{r}, \mathbf{q}\sigma) = \sum_{\mathbf{a},\kappa} \delta\zeta_\kappa^{\mathbf{a}}(\mathbf{q}, \sigma)\rho_\kappa(\mathbf{r} - \mathbf{R}_\kappa^{\mathbf{a}}). \qquad (20)$$

The CF's $\delta\zeta_\kappa^{\mathbf{a}}$ in equation (20) are obtained from equation (12) and the form-factors from equation (2).

In contrast to the constraint for O_z^Γ expressed by equation (19) no such restriction must be satisfied in the metallic phase for O_z^Z. While in O_z^Γ only an *intracell* CT is allowed summing up to zero, O_z^Z generates CF's of the same sign in the cell (table 3). This finally leads to CF's of alternating sign in consecutive RuO layers (cells), i.e. an *interlayer (intercell)* CT is set up, see also figure 11. The latter provides an effective screening mechanism of the Coulomb interaction and explains the strong renormalization of O_z^Z as compared with O_z^Γ.

In the adiabatic approximation used in the calculations so far the interlayer CT is instantaneous. It has to be replaced by a dynamic collective charge transfer in case a phonon–plasmon scenario would be realistic as for La_2CuO_4 in a nonadiabatic region nearby the c-axis. The question if such a scenario is

also likely for the more anisotropic Sr_2RuO_4 is discussed in section 3.3.

An important difference is found when considering the OBSM in the cuprates and in Sr_2RuO_4, respectively. The anomalous softening of the OBSM phonon anomalies, see figure 12(a), in particular of the half breathing mode $\Delta_1/2$ which is typical for La_2CuO_4 [8], and most probably generic for all the cuprate-based HTSC's [9, 31] is strongly reduced in our calculation as compared with La_2CuO_4. In the experiments the softening is completely absent, see figure 12(b). Our calculations show that there is a dominant microscopic reason for the vanishing of the OBSM anomalies in Sr_2RuO_4, namely the magnitude of the on-site Coulomb repulsion $U(Ru\,4d)$ of the 4d orbitals of ruthenium. The latter is obviously underestimated in our *ab initio* calculation based on the ionic form-factor ρ_κ. Compared with the calculated value for the on-site repulsion $U(Cu\,3d) = 1.005$ dRyd in La_2CuO_4 which leads to good results for the frequencies of the OBSM in this material, the calculated value for ruthenium, $U(Ru\,4d) = 0.619$ dRyd, seems not so reliable because of the more incomplete 4d shell of Ru and the spherical average assumed in our computations for the orbital densities. So, we increased the value of the Ru 4d on-site repulsion in two steps towards the calculated result for the Cu 3d orbital for comparison. As a consequence the phonon anomalies completely vanish in these calculations in agreement with experiment as displayed in figure 12(b). Simultaneously by increasing U(Ru 4d) the CF's on the Ru 4d orbitals that are a measure for the nonlocal electron–phonon coupling are strongly decreased as can be seen in table 4.

In [32] and [33] sharply peaked magnetic fluctuations at $\mathbf{q}_0 = 0.6\frac{\pi}{a}(1, 1, 0)$ have been observed for Sr_2RuO_4. These
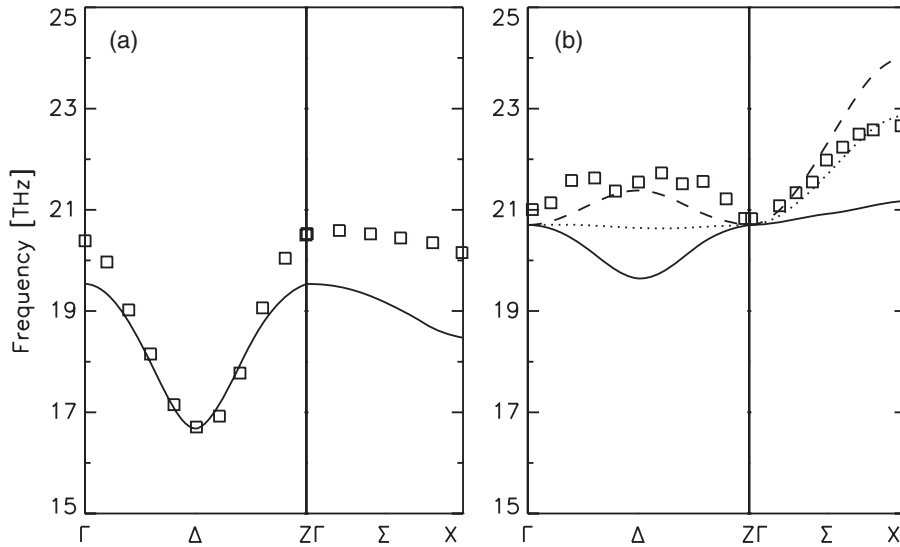
Figure 12. Calculated dispersion of the highest Δ_1 and Σ_1 branch in La$_2$CuO$_4$ [8] (a) and Sr$_2$RuO$_4$ (b). In (b) these branches have been obtained for three different values of the on-site repulsion U(Ru 4d) of the Ru 4d orbitals and are characterized by different line types, U(Ru 4d) $= 0.619$ dRyd (——), U(Ru 4d) $= 0.769$ dRyd ($\cdots$) and U(Ru 4d) $= 1.005$ dRyd (– – –). The experimental values are indicated as open squares ($\square$) [11].

Table 4. Calculated magnitudes of the charge fluctuations $|\delta\zeta_\kappa|$ in units of 10^{-3} particles on the Ru 4d orbitals generated by the $\Delta_1/2$ and the O$_B^X$ mode in dependence of the on-site Coulomb repulsion U(Ru 4d). ν is the frequency of the mode in units of THz. The results are listed from left to right taking for U(Ru 4d) 0.619, 0.769 and 1.005 dRyd. The latter value matches the calculated value of U for the Cu 3d orbital in La$_2$CuO$_4$ and the first value is the calculated *ab initio* result for the Ru 4d orbitals.

	$\Delta_1/2$			O$_B^X$		
$|\delta\zeta_{\text{Ru 4d}}|$	38.252	26.603	17.871	50.875	33.764	22.048
ν	19.635	20.642	21.381	21.178	22.875	24.031

fluctuations have been related to dynamical nesting properties between the flat α and β sheets of the FS, compare with figure 5(a). Braden *et al* [11] have performed a search for Kohn anomalies in the phonon spectrum related to this nesting structure. Promising candidates would be the high-frequency Σ_1 modes which are coupled to the Ru 4d CF's. However no signature for a Kohn anomaly is present in the experiments as well as in the calculation in figure 10. Another possibility discussed in [11] is the longitudinal acoustic Σ_1 branch where a small dip is observed just around $\mathbf{q}_0$, see figure 13. From our calculations it seems very unlikely that this dip is a nesting effect because our computations of the phonon dispersion shows that this feature is well described by a complex anticrossing between the three lowest branches with Σ_1 symmetry, as shown in figure 13. So we do not find in Sr$_2$RuO$_4$ any evidence for EPI driven by nesting of the FS.

3.3. Search for a phonon–plasmon scenario in Sr$_2$RuO$_4$

We investigate for Sr$_2$RuO$_4$ the possibility of a phonon–plasmon scenario along the c-axis and in a small region around this axis by performing calculations of the coupled electron–phonon dynamics in the nonadiabatic regime. This is achieved
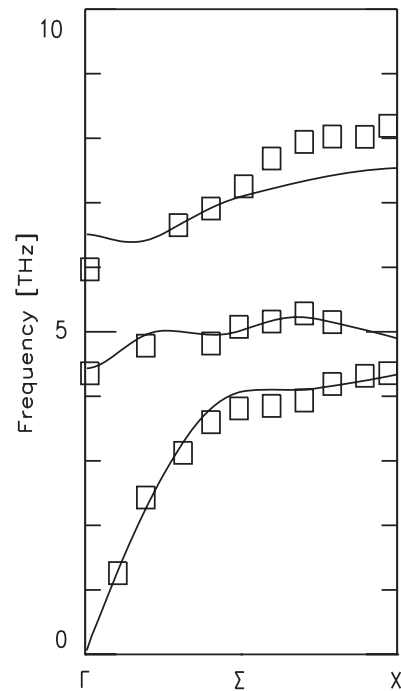

Figure 13. Calculated phonon dispersion in the M27BM2 of the three lowest Σ_1 branches displaying a complex anticrossing behaviour. The open squares ($\square$) are the experimental data [11].

approximatively by allowing the proper polarization part $\Pi_{\kappa\kappa'}$ of the DRF to depend on the frequency of the perturbation. Different from *static screening* in the adiabatic approximation this leads to *dynamical screening* of the Coulomb interaction. A nonadiabatic treatment of the charge response and a related phonon–plasmon coupling has been shown recently to be a realistic option for La$_2$CuO$_4$ if the real anisotropy of the material is taken into account in the theory [12].
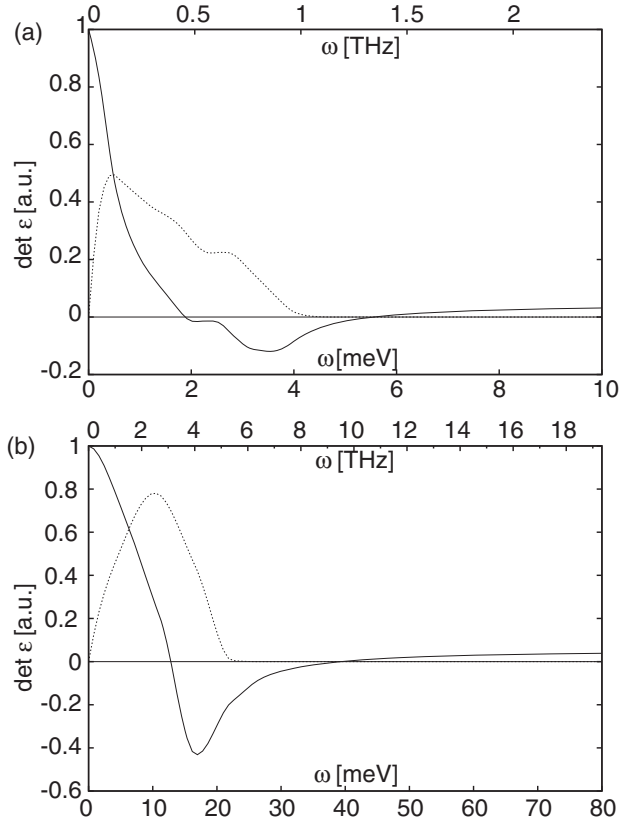
Figure 14. Real- and imaginary part of $\det[\varepsilon_{\kappa\kappa'}(\mathbf{q}, \omega)]$ at the Z point in arbitrary units for Sr_2RuO_4 in the M27BM2 (a) and for La_2CuO_4 in the M31BM [12] (b). The real part is given by the full line (——) and the imaginary part by the dotted line ($\cdots$).

Figure 15. Calculated nonadiabatic coupled phonon–plasmon dispersion within the M27BM2. (a) Λ_1 modes (——) in the collisionless regime, the coupling modes at Γ (A_{2u}^Γ (ferro, na)) and at Z (O_z^Z (na)) are shown as black dots (●). (b) Δ_1' modes (——) along the Δ' ($= (\varepsilon\frac{2\pi}{a}, 0, \frac{2\pi}{c})$ direction from Z ($\varepsilon = 0$) to Z' ($\varepsilon = 0.02$). The black dot (●) at Z and Z' are the O_z^Z (na) and approximately the O_z^Z mode in adiabatic approximation, respectively. In both figures the broken line (– – –) denotes the free-plasmon branch and the dotted line ($\cdots$) the borderline for damping due to electron–hole decay.

Due to the much weaker k_z-dispersion of the electronic band structure obtained in the computation for Sr_2RuO_4 as compared with La_2CuO_4 we can expect much lower plasmon frequencies along the c-axis. This conjecture can be shown to be true for example by calculating at the Z point the free-plasmon frequency according to equation (15) and checking the result against La_2CuO_4, see figure 14. From the zero crossing of the real part and the vanishing of the imaginary part of $\det[\varepsilon_{\kappa\kappa'}(Z, \omega)]$ we get for Sr_2RuO_4 in the M27BM2 the very small value of $\omega_p(Z) = 5.55$ meV (1.342 THz) while for La_2CuO_4 we have $\omega_p(Z) = 39.33$ meV (9.509 THz) [12] which is by a factor of seven larger. This also expresses the much stronger anisotropy of Sr_2RuO_4 in relation to the cuprates.

In the analysis of the phonon–plasmon scenario we have assumed the collisionless regime, i.e. the quasiparticles (QP) do not scatter each other and damping is only possible via intraband electron–hole decay and low lying interband transitions. However, in the cuprates and also in Sr_2RuO_4 QP scattering due to electron–electron interaction and other degrees of freedom is certainly important. This leads to damping and possibly overdamping of c-axis plasmons at sufficiently low frequencies and so the latter may cease to be well defined collective excitations of the Fermi liquid.

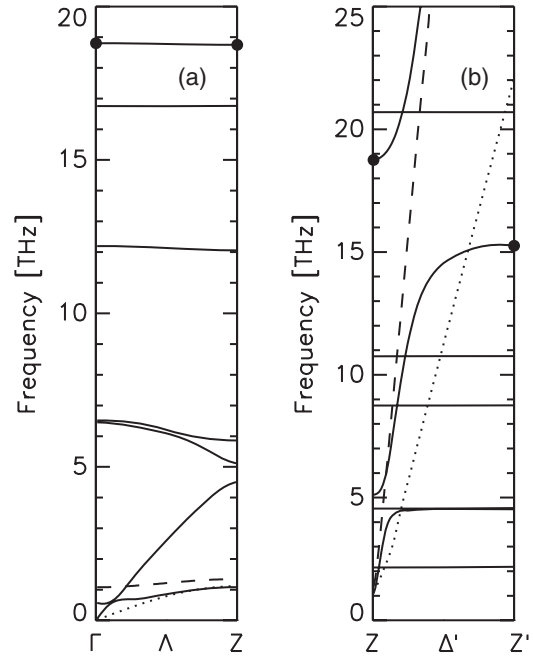In order to make an estimate of the range of frequencies where c-axis plasmons should exist we examine the zero crossing of the real part of the well known dielectric function of an electron gas

$$\varepsilon(\omega) = \varepsilon_\infty - \frac{\omega_p^2}{\omega^2 + \gamma^2}. \qquad (21)$$

ε_∞ is the high-frequency dielectric constant, $\gamma = \frac{1}{\tau}$ the scattering rate of the QP's along the c-axis. Equating $\varepsilon(\omega)$ to zero we have the equation,

$$\omega^2 = \frac{\omega_p^2}{\varepsilon_\infty} - \gamma^2. \qquad (22)$$

Using for γ the value given in [34] ($\gamma = 170$ cm^{-1}) in the normal state of La_2CuO_4 and the calculated value for the high-frequency dielectric constant along the c-axis $\varepsilon_\infty^{zz} \approx 2$ [19] we obtain $\omega^2 \geqslant 0$ for $\omega_p \geqslant 7.21$ THz. For smaller plasmon frequencies we have $\omega^2 < 0$, i.e. the plasmon has a diffusive pole and hence the c-axis plasmon is overdamped in the normal state. It should be remarked that larger values for ε_∞^{zz} would increase the critical value for ω_p beyond that the plasmon could exist. For example setting $\varepsilon_\infty^{zz} = 3$ or $\varepsilon_\infty^{zz} = 4$ we would have $\omega_p \geqslant 8.83$ THz or 10.19 THz, respectively. Assuming a similar c-axis scattering rate of the QP's for Sr_2RuO_4 we regard $\omega_p \approx 7$ THz as a reasonable limiting frequency beyond which plasmons most likely are not overdamped.

Thus, from our calculations of the plasmon along the c-axis (Λ direction) displayed in figure 15(a) which are at very

low frequencies around 1 THz we conclude that the latter are overdamped. On the other hand at larger plasmon frequencies which result in case the wavevector **q** is not strictly parallel to the c-axis, as shown for example in figure 15(b), the plasmon can acquire enough energy to resist overdamping and may exist as a collective excitation.

In figure 15(a) we identify instead of the six Λ_1 branches of the adiabatic approximation (compare with figure 2(c)) an additional branch due to phonon–plasmon coupling. The free-plasmon has frequencies around 1 THz and is nearly dispersionless along the Λ direction. This is in contrast with the situation in La_2CuO_4 [12] where the free-plasmon has significant higher frequencies and increases from about 9.5 THz at the Z point to about 12.8 THz at Γ. Thus, the plasmon is not overdamped along the c-axis in La_2CuO_4 while the phonon–plasmon scenario calculated in the collisionless regime for Sr_2RuO_4 as displayed in figure 15(a) is not realistic.

Analogous to the situation in La_2CuO_4 [6, 12] the calculated free-plasmon frequencies rapidly increase in proportion to the transverse component of the **q** vector in a small nonadiabatic region of the charge response around the c-axis. We have performed calculations along the $\Lambda'' = (\varepsilon\frac{2\pi}{a}, 0, \zeta\frac{2\pi}{c})$ and $\Lambda' = \zeta(\varepsilon\frac{2\pi}{a}, 0, \frac{2\pi}{c})$ direction in this region, see figure 16, for different small ε-values to study a possible phonon–plasmon scenario in Sr_2RuO_4. We do not go into the details of these computations here but what is important concerning the question of overdamping is that for $\varepsilon \geqslant 0.0040$ in case of the Λ' direction and for $\varepsilon \geqslant 0.0025$ in the Λ'' direction the free-plasmon frequency is larger than 7 THz, the estimated value for the phonon–plasmon scenario to exist. From the calculations we find that the longitudinal A_{2u}^{Γ} (ferro, na) mode at Γ (figure 15(a)) is virtually unchanged at $\varepsilon = 0.0040$ and so does exist around 19 THz. The same holds true for O_z^Z (na) at the Z point being practically the same as $O_z^{Z'}$ for $\varepsilon = 0.0025$ in the Λ'' direction. Similar as for La_2CuO_4 [12] with increasing ε A_{2u}^{Γ} (ferro, na) and $O_z^{Z'}$ (na) rapidly leave the spectrum to high frequencies.

In case of $O_z^{Z'}$ (na) this mode behaviour can also be extracted from figure 15(b) where we have presented our calculated results of the dispersion of the coupled phonon–plasmon Δ_1' modes along the $\Delta' = (\varepsilon\frac{2\pi}{a}, 0, \frac{2\pi}{c})$ direction from $Z = (0, 0, \frac{2\pi}{c})$ to $Z' = (\varepsilon\frac{2\pi}{a}, 0, \frac{2\pi}{c})$ for $0 \leqslant \varepsilon \leqslant 0.02$. The highest mode at Z is the O_z^Z (na) mode also seen in figure 15(a) as a black dot. The broken line is the dispersion of the free-plasmon branch calculated from equation (15) and the dotted line is the borderline for damping due to electron–hole decay investigated from $\max_{\mathbf{k}\in BZ} (E_n(\mathbf{k}) - E_n(\mathbf{k} + \mathbf{q}))$ for the bands crossing the Fermi level. From this figure the range of the region with a nonadiabatic charge response can be estimated. It is characterized by the steep branch which ultimately converges to the frequency of the adiabatic O_z^Z mode (black dot at Z'). Similar as in La_2CuO_4 this nonadiabatic region is very small and can be estimated from the figure at about $\varepsilon = 0.01$. Unlike the case of La_2CuO_4 the phonon–plasmon dispersion in figure 15(b) should not exist in the full range of frequencies according to our estimate for overdamping below about 7 THz.

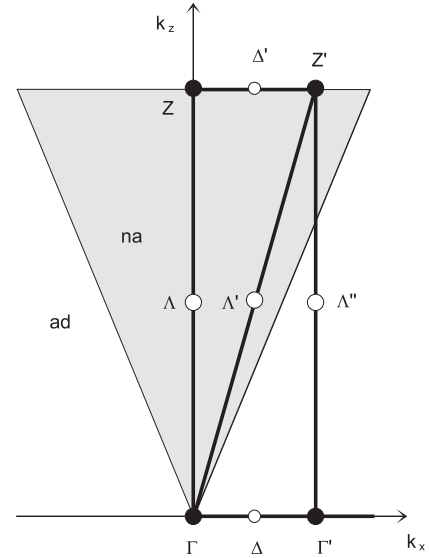Parallel to the investigation of the O_z^Z mode in La_2CuO_4 [6, 12], the line-broadening of this mode observed

Figure 16. Schematic representation of the nonadiabatic region in the (k_x, k_z) plane with the directions $\Delta' = (\varepsilon\frac{2\pi}{a}, 0, \frac{2\pi}{c})$, $\Lambda' = \zeta(\varepsilon\frac{2\pi}{a}, 0, \frac{2\pi}{c})$ and $\Lambda'' = (\varepsilon\frac{2\pi}{a}, 0, \zeta\frac{2\pi}{c})$. $\zeta \in [0, 1]$. na: nonadiabatic region; ad: adiabatic region.

by [11] in Sr_2RuO_4 can be understood from the calculated phonon–plasmon scenario. Experimentally there is a limited wavevector resolution in INS for the transverse direction perpendicular to the c-axis which for the experiments in La_2CuO_4 is on the average $\varepsilon = 0.03$ [35]. Thus, the relevant frequency range sampled in the measurement for O_z^Z is over the steep branch beyond which the mode develops an $O_z^{Z'}$-like displacement pattern. According to the calculations this sampling occurs for mode frequencies larger than 12.5 THz and leads to a corresponding broadening of the linewidth for O_z^Z observed in the experiment.

Because the region with a metallic adiabatic charge response outweighs by a factor of roughly three the nonadiabatic region we can attribute to the O_z^Z mode an adiabatic frequency of about 15.3 THz. The Δ_1' branch starting at O_z^Z (na) in figure 15(b) has not been observed in the experiments so far because a very high **q**-space solution transverse to the c-axis would be needed to resolve the mode dispersion in the small nonadiabatic sector.

In [12] we have pointed out for La_2CuO_4 the relevance of a strongly coupling nonadiabatic O_z^Z mode. So it is interesting to see if such a large EPI also exists for O_z^Z (na) in Sr_2RuO_4. As a parameter for the strength of the EPI in a certain mode $(\mathbf{q}\sigma)$ we have used in the past the orbital averaged changes of the self-consistent crystal potential $\delta V_\kappa(\vec{q}\sigma)$, [6, 12]. In case of La_2CuO_4 we obtain in units of meV $|\delta V_{Cu\ 3d}| = 955.98$ and $|\delta V_{O\ 2p}| = 515.98$ which should be compared with the considerably reduced strength $|\delta V_{Ru\ 4d}| = 277.24$ and $|\delta V_{O\ 2p}| = 316.64$ in Sr_2RuO_4.

Altogether, we conclude from our calculations for Sr_2RuO_4 that nonadiabatic EPI via phonon–plasmon coupling is not possible strictly along the c-axis but most likely away from this axis in a very small region at higher free-plasmon frequencies. Moreover, the strength is significantly smaller as in La_2CuO_4.

We have argued above that the longitudinal ferroelectric A_{2u}^{Γ} (ferro, na) mode exists in the nonadiabatic sector around the Γ point at about 19 THz. This nonadiabatic result helps to understand why c-axis optical activity seen in the experiments [36] is possible despite the fact that Sr_2RuO_4 is in the metallic phase. In [36] three c-polarized A_{2u} phonon structures at 6.04, 10.88 and 14.51 THz have been detected which agree well with the calculated transverse A_{2u}^{Γ} modes in the M27BM2 at 5.16, 10.42 and 14.49 THz. The by far largest oscillator strength is obtained for the mode at 10.88 THz and according to our calculation this is the ferroelectric mode A_{2u}^{Γ} (ferro). Consistent with the large oscillator strength of this mode in the experiment our nonadiabatic result for the longitudinal ferroelectric mode A_{2u}^{Γ} (ferro, na) predicts a very large A_{2u} splitting of about 9 THz. This splitting dominates the infrared response for polarization along the c-axis. Further we find in the calculations two other longitudinal A_{2u} modes at 12.379 and 6.964 THz which define corresponding splittings with the transverse modes above.

From a theoretical point of view it is important to remark that optical activity in the metallic phase cannot be explained using the adiabatic approximation for a calculation of the phonon dispersion as is commonly done by applying static DFT for the metal [22–25]. In such calculations there will be no LO–TO or A_{2u} splittings being a measure for the oscillator strength because the transverse effective charges vanish if the metallic phase is treated in adiabatic approximation and consequently the induced dipole moments defining the oscillator strength in the dielectric matrix vanish too. Thus, there will be no optical activity in a metal by the phonons treated in adiabatic approximation which underlies static DFT.

4. Summary and conclusions

We have shown that for a reliable description of the c-axis charge response in Sr_2RuO_4 and in particular the phonon dynamics along this axis a typical LDA-based model is too isotropic and must be modified to account for the much weaker interlayer coupling in the real material. Similar as in the cuprates studied earlier the large anisotropy in Sr_2RuO_4 is considerably underestimated in DFT–LDA calculations of the electronic BS.

From our investigations we conclude that an accurate representation of the very fainty k_z-dispersion of the BS nevertheless is essential to understand the c-axis polarized Λ_1 modes. While the LDA-based model (27BM) is insufficient a modified much more anisotropic model (M27BM2) is well suited.

We have examined the multi-sheet FS of Sr_2RuO_4 with the two models and found that the experimental results for the FS are not well described within the 27BM. On the other hand, the M27BM2 shows a good agreement with the measured FS. This model can be considered to represent the real anisotropy in Sr_2RuO_4 sufficiently well.

We have also calculated the magnitude of the strongly enhanced anisotropy in the M27BM2 compared with the 27BM more globally in terms of some Fermi surface parameters important for transport properties. Checking both models against each other we find an enhancement of about a factor

18 for the anisotropy ratio of the Drude plasma energy tensor and of about a factor of 10 for the Fermi velocity tensor. While the calculations demonstrate that Sr_2RuO_4 is a nearly two-dimensional Fermi liquid significantly more anisotropic than La_2CuO_4 the remaining very weak three-dimensionality is crucial to achieve a solid representation of the c-axis charge response and of certain c-axis phonons.

We have calculated in detail the phonon dispersion in Sr_2RuO_4 along the main symmetry directions in the BZ and compared the result with the dispersion of the HTSC La_2CuO_4 being structural isomorphic. A good overall agreement of the calculated results is found for Sr_2RuO_4 with the INS data. Comparing the results of the calculated phonon dynamics in the RIM with a model allowing additional DF's and finally the full model including DF's and CF's the renormalization of certain modes which are strongly coupled via nonlocal EPI effects of DF and CF type has been analysed in detail. In this context an important point of the comparison with La_2CuO_4 is that the anomalous softening of the high-frequency oxygen bond-stretching modes, being generic for the cuprate-based HTSC's, is strongly reduced or completely absent in Sr_2RuO_4 depending primarily on the magnitude of the on-site Coulomb repulsion of the Ru 4d orbitals.

We have also investigated the possibility of a Kohn anomaly in the Σ_1 modes of Sr_2RuO_4 as discussed in the literature. In our calculations we do not find any evidence for such an anomaly driven by nesting of the FS. Instead, the dip in the lowest Σ_1 branch seen in the experiments is well explained in our computations by an anticrossing effect of the three lowest Σ_1 branches.

Finally, we have examined the question of a possible phonon–plasmon scenario in a small region of nonadiabatic charge response around the c-axis which has been shown to be a realistic option in La_2CuO_4.

Due to the much weaker electronic k_z-dispersion obtained for Sr_2RuO_4 the calculated free-plasmon frequencies along the c-axis are about a factor of eight smaller in the collisionless regime than in La_2CuO_4. We have argued that damping generated by the interactions between the QP's as well as interband transitions which are at much lower energy scale than in La_2CuO_4 leads to an overdamping of the plasmon strictly along the c-axis in contrast to La_2CuO_4. However, a coupled phonon–plasmon scenario becomes likely also in Sr_2RuO_4 at higher free-plasmon frequencies. This occurs in case the wavevector is not strictly parallel to the c-axis but has a small transverse component. We find that the strength of this nonlocal nonadiabatic coupling is significantly weaker than in La_2CuO_4.

Ultimately we have explained by our calculations of the nonadiabatic charge response the linewidth of the apex oxygen breathing mode at the Z point and why c-axis optical activity as seen in the experiments is possible despite the fact that Sr_2RuO_4 is in the metallic phase.

References

[1] Maeno Y *et al* 1994 *Nature* **372** 532
[2] Bergemann C, Mackenzie A P, Julian S R, Forsythe D and Ohmichi E 2003 *Adv. Phys.* **52** 639

[3] Ho A F and Schofield A J 2005 *Phys. Rev.* B **71** 045101
[4] Mackenzie A P and Maeno Y 2003 *Rev. Mod. Phys.* **75** 657
[5] Mao Z Q *et al* 2003 *Phys. Rev.* B **63** 144514
[6] Falter C 2005 *Phys. Status Solidi* b **242** 78
[7] Bauer T and Falter C 2008 *Phys. Rev.* B **77** 144503
[8] Falter C, Bauer T and Schnetgöke F 2006 *Phys. Rev.* B **73** 224502
[9] Pintschovius L 2005 *Phys. Status Solidi* b **242** 30
[10] Falter C, Klenner M and Ludwig W 1993 *Phys. Rev.* B **47** 5390
[11] Braden M, Reichardt W, Sidis Y and Maeno Y 2007 *Phys. Rev.* B **76** 014505
[12] Bauer T and Falter C 2009 arXiv:0808.2765[cond-mat]
[13] Alexandrov A S 1992 *Phys. Rev.* B **46** 2838
[14] Falter C, Klenner M, Hoffmann G A and Schnetgöke F 1999 *Phys. Rev.* B **60** 12051
[15] Falter C 1988 *Phys. Rep.* **164** 1
[16] Falter C, Klenner M and Hoffmann G A 1995 *Phys. Rev.* B **52** 3702
[17] Alexandrov A S 1996 *Phys. Rev.* B **53** 2863
[18] Hardy T M, Hague J P, Samson J H and Alexandrov A S 2009 *Phys. Rev.* B **79** 212501
[19] Falter C and Schnetgöke F 2002 *Phys. Rev.* B **65** 054510
[20] Perdew J P and Zunger A 1981 *Phys. Rev.* B **23** 5048
[21] Krakauer H, Pickett W E and Cohen R E 1998 *J. Supercond.* **1** 11
[22] Savrasov S Y and Andersen O K 1996 *Phys. Rev. Lett.* **77** 4430
[23] Wang C Z, Yu R and Krakauer H 1999 *Phys. Rev.* B **59** 9278
[24] Bohnen K P, Heid R and Krauss M 2003 *Europhys. Lett.* **64** 104
[25] Giustino F, Cohen M L and Louie S G 2008 *Nature* **452** 975
[26] Mazin I I, Papaconstantopoulos D A and Singh D J 2000 *Phys. Rev.* B **61** 5223
[27] Shen K M *et al* 2007 *Phys. Rev. Lett.* **99** 187001
[28] Chmaissem O *et al* 1998 *Phys. Rev.* B **57** 5007
[29] Moore R G *et al* 2008 *Phys. Rev. Lett.* **100** 066102
[30] Uruma M *et al* 2008 arXiv:0711.2160[cond-mat] (unpublished)
[31] Graf J *et al* 2008 *Phys. Rev. Lett.* **100** 227002
[32] Sidis J *et al* 1999 *Phys. Rev. Lett.* **83** 3320
[33] Braden M *et al* 2002 *Phys. Rev.* B **66** 064522
[34] Tamasaku K, Nakamura Y and Uchida S 1992 *Phys. Rev. Lett.* **92** 1455
[35] Pintschovius L, private communication
[36] Katsufuji T, Kasai M and Tokura Y 1996 *Phys. Rev. Lett.* **76** 126